High Strain Rate Deformation of Aged TRIP Ti-10V-2Fe-3Al (wt.%) Examined by In-situ Synchrotron X-Ray Diffraction

November 18, 2022

Authors: B. Ellyson[a*], A. Saville[a] K. Fezzaa[b], T. Sun[b], N. Parab[b], C. Finfrock[a], C.J. Rietema[a], D. Smith[a], J. Copley[a], C. Johnson[a], C.G. Becker[a], J. Klemm-Toole[a], C. Kirk[c], N. Kedir[d], J. Gao[c], W. Chen[c,d], K.D. Clarke[a] A.J. Clarke[a]

[a]George S. Ansell Department of Metallurgical and Materials Engineering, Colorado School of Mines, Golden, Colorado

[b]The Advanced Photon Source, Argonne National Laboratory, Lemont, Illinois

[c]School of Aeronautics and Astronautics Engineering, Purdue University, West-Lafayette, Indiana

[d]School of Advanced Materials Engineering, Purdue University, West-Lafayette, Indiana

[*]Corresponding author: bellyson@mines.edu

1 Abstract

Transformation Induced Plasticity (TRIP) is a promising avenue for tailoring the work hardening response of metastable β titanium (Ti) alloys. Here we show that aged TRIP Ti-10V-2Fe-3Al (wt.%) maintains higher elongations and flow stresses as strain rate increases, if phase stability and microstructural characteristics are tuned. Low temperature aging influences the matrix β phase stability by ω phase precipitation, which affords a promising way to impact the TRIP effect and obtain desirable mechanical properties, ranging from high damping capacity to good strength/ductility combinations. Although TRIP is active during quasi-static and dynamic testing up to 2000 s^{-1}, increasing aging time and/or strain rate reduces the overall propensity for the TRIP effect and extent of transformation, which occurs rapidly just at the onset of yielding. TRIP with ω phase precipitation provides interesting alloying, microstructure, and property design strategies for engineering applications like lightweight protective structures, where high strains and the need

for energy absorption are encountered.

2 Introduction

Titanium (Ti) alloys are heavily used in the aerospace and defense sectors for structural components to leverage their high strength to weight ratios. While providing high strengths, $\alpha + \beta$ microstructures typically exhibit low work hardening rates and limited uniform elongation [1]. TRansformation Induced Plasticity (TRIP), or the formation of martensite from the metastable parent β phase, provides a way to improve the work hardening characteristics of Ti alloys. Blast armor is an example engineering application of Ti alloys in the defense sector [2], where the TRIP effect may be beneficially used to provide increased survivability. Due to the superior formability of metastable β Ti alloys, the production of more complex cold-formed parts also becomes possible. TRIP is also known to produce simultaneously strong and ductile advanced high strength steel grades for automotive applications [3]. Although Ti alloys have long been known to exhibit the TRIP effect, opportunity exists to exploit TRIP in these alloys to improve their work hardening characteristics and create interesting strength/ductility combinations [4]. Understanding the TRIP effect in Ti alloys and the dependence of TRIP on factors such as temperature, strain rate, and strain path are crucial to effectively designing phase stability and microstructures that exhibit TRIP during deformation.

TRIP Ti alloys have been reported to exhibit low yield stresses, due to a low transformation stress, leading to the onset of martensite formation prior to yielding of the β phase matrix from slip [5]. However, recent publications have demonstrated the strong effect that short-time, low-temperature aging has on yield strength and ductility of TRIP-exclusive [4] and TRIP/TWinnng Induced Plasticity (TWIP) Ti alloys [6]. For example, early-stage aging of athermal ω phase precipitates, in combination with TRIP, has been shown to produce high yield strengths and uniform elongations in the alloy Ti-10V-2Fe-3Al (wt.%) (Ti-1023) [4]. **Aging at temperatures below the metastable solvus for ω phase has been found to lead to coarsening of the athermally formed precipitates, leading to significant strengthening combined with TRIP , while avoiding the well-known brittle behavior reported for longer aging times (10s of hours) and higher temperatures (up to 573 K) . While the fundamental mechanism is still not well understood, omega-phase strengthening through early stage aging is a novel strengthening strategy for metastable β Ti alloys and requires significantly more work to address some of the challenges presented by short times and low temperatures involved. Additionally, initial reports on the behavior have raised**

important questions as to the thermal stability of $beta$ **Ti alloys presenting TRIP and TRIP/TWIP enabled microstructures and the** ω **phase that will have to be addressed for long-term use of these microstructural states [4].** Early evidence also suggests that two-phase $\alpha + \beta$ microstructures can exhibit TRIP during deformation, providing improved work hardening and yield strengths [7, 8]. Significant opportunity exists to better understand TRIP in metastable Ti alloys, given the promising nature of $\beta + \omega$ and $\beta + \alpha$ TRIP microstructures to produce good mechanical properties.

If TRIP, TWIP, or TRIP/TWIP Ti alloys are to be designed for impact/blast resistance or formability, further knowledge of their dynamic response is needed. While extremely useful for initial understanding of TRIP, quasi-static properties may be inherently problematic for designing microstructures for high strain rate mechanical response. To the authors' knowledge, only a few studies [9, 10] have been published on the dynamic response and microstructure evolution of metastable Ti alloys. Only alloys exhibiting TRIP and TWIP (TRIP/TWIP) have been studied at elevated strain rates up to 10^3 s^{-1} in compression [9, 10]. The high strain rate deformation of TRIP-exclusive alloys is absent from the literature, particularly in tension. Here we examine low-temperature aging and microstructure evolution in ($\beta + \omega$) TRIP Ti-1023 during high strain rate tensile deformation. In-situ synchrotron **X-ray** diffraction was performed to understand the TRIP effect at strain rates up to 2000 s^{-1}, along with complementary electron microscopy.

3 Methodology

3.1 Sample Preparation, Conventional Mechanical Testing, and Microstructure Characterization

A hot-rolled Ti-1023 bar 50.8 mm in diameter was received from ATI in the $\alpha + \beta$ condition. The chemistry, determined by inductive coupled plasma mass spectrometry, is provided in Table 1. Conventional machining was performed to produce miniature high strain rate tensile specimens with a gage cross-section of 0.5×1 mm^2 (see Supplementary Materials) for testing at the Advanced Photon Source (APS) at Argonne National Laboratory (ANL) (described later). The tensile axis was aligned with the rolling direction in all cases. Some variation in texture was observed, due to the sample extraction strategy, as further discussed in the Supplementary Materials. The miniature tensile specimens were ground to final thickness of 0.5 mm using 320 grit SiC metallographic paper.

All tensile specimens were cleaned, wrapped in Ta foil, and encapsulated under vacuum in

Table 1: Chemistry of the as-received Ti-1023 material in wt. %.

V	Fe	Al	O	C	N	Ti
9.97	1.88	2.77	0.12	0.02	0.01	Bal.

quartz tubes for heat treatment to minimize contamination and oxygen pick-up. The solutionizing heat treatment consisted of an isothermal hold at 1123 K for 30 min. All specimens were immediately quenched into room temperature water by breaking each capsule underwater. The resulting microstructure was single phase β, with equiaxed grains and an average grain size of $\sim$100 μm, as determined by electron backscatter diffraction (EBSD).

Three conditions were produced for this study: as-quenched (AQ) (solution treated, no intentional aging), maximum TRIP strength (MTS), and TRIP Inhibited (TI). The MTS and TI conditions were produced by aging in a closed-loop controlled synthetic oil bath at 423 K for 900 s or 7200 s, respectively. These aging times were selected based upon previous work [4] to achieve different strength/ductility combinations and ω phase coarsening plus TRIP. The MTS condition exhibits an optimal strength/ductility combination, whereas the TI condition has maximum strength, but ductility loss. Aging times beyond 1800 s were found to reduce TRIP activity and ductility [4]. Chemical analysis after the heat treatments revealed no measurable composition changes compared to the as-received condition.

Quasi-static tensile testing was conducted at the Colorado School of Mines on an electromechanical Alliance load-frame at a strain rate of 10^{-3} s^{-1} with a 25 mm Shepic-type extensometer. Intermediate strain rate testing was performed on a hydraulic MTS load-frame with a 25 mm MTS blade-type extensometer. All quasi-static and intermediate strain rate testing was performed on ASTM E8 subsized [11] tensile specimens with a gauge length of 25.4 mm and cross-section of 3.175×6.35 mm^2.

Specimens for Electron Backscatter Diffraction (EBSD) were prepared by electropolishing at 20 V and 253 K, with a mixture of 6 % perchloric and 4 % hydrochloric acid diluted with a 2:1 mixture of methanol and butoxyethanol. EBSD scans were performed in a FEI Helios 600i dual-column Focused Ion Beam (FIB)/Scanning Electron Microscope (SEM), an accelerating voltage of 20 kV, beam current of 11 nA, and step size of 1 μm. No post-scan clean-up procedures were applied to the results.

After post-scan analysis of EBSD results, reconstruction of pre-transformed β-Ti microstructures was completed using the MATLAB plugin MTEX Version 5.70 [12]. This process employed a triple-point based voting reconstruction algorithm [13] to back-calculate parent grains prior to deformation and evaluate the response of different deformation mechanisms as a function of parent β-Ti grain orientation. The reconstruction process started with the previously reported orientation relationship (OR) between α'' and β-Ti [14]. This orientation relationship was subsequently optimized for the data acquired in each EBSD scan using the MTEX add-on ORTools [13]. For the reconstructions reported in this work, the optimized OR was $\{12\bar{2}\}_{\beta} \parallel \{210\}_{\alpha''}$ and $< 01\bar{1}_{\beta} > \parallel < 001_{\alpha''} >$. Data processing of the as-transformed EBSD maps was completed prior to implementing the reconstruction algortihm. This consisted of calculating unique grains with a grain boundary misorientation threshold of 2°, removing any grains less than two pixels in size, recalculating the filtered grains with 1.5° misorientation thresholds, and completing a smoothing plus filling process with a half quadratic filter set to 0.5. During calculations for parent grain reconstruction, a voting fit of 2.5-5° was set when evaluating triple points, a minimum probability of 0.7 was set for determining if a reconstruction calculation was valid, and the growth of parent grains at boundaries was set to a 2.5° threshold. Further processing of merging parent grains with less than 5° misorientations and merging reconstructed inclusions less than two pixels in size was also completed. Calculation of grains in the reconstructed microstructure was completed with a 3° misorientation threshold and removing any parent grains less than 70 pixels in size. A half quadratic filter of 0.25 was also applied to fill and smooth the reconstructed parent microstructures. Schmid factor calculations for the reconstructed microstructures were also completed using MTEX Version 5.70. The slip system used for Schmid factor calculations was $\{110\}_{\beta} < 111 >_{\beta}$, and the system used for the shear component of the α" transformation was $\{112\}_{\beta} < 111 >_{\beta}$.

3.2 In-Situ Synchrotron X-Ray Diffraction and High Strain Rate Testing

In-situ synchrotron x-ray imaging and diffraction were performed during high strain rate (modified Kolsky) pressure bar testing at Sector 32-ID-B at the Advanced Photon Source (APS) at Argonne National Laboratory (ANL), in Lemont, Illinois, USA. The details of the Kolsky bar setup have been reported elsewhere [15, 16, 17, 18]. A "pink-beam" condition was used, with a maximum flux at a wavelength of 0.512 and a characteristic, asymmetric intensity profile near the harmonic energies. A beam size of 2 mm wide by 1 mm in height was used to illuminate the gauge length of the miniature tensile specimens. Different detector positions were used to obtain specific resolution and ranges in q-space. Standards of pure Al and pure Ta foil were used to calibrate the detector position. Ta was particularly useful, as the crystal structure (BCC) and lattice parameter are similar to the β phase in Ti alloys. Analysis of the raw diffraction data was completed using High Speed Polychromatic Diffraction (HiSPoD), a MATLAB program developed at Sector 32-ID. Additional details are given elsewhere [19].

The (modified Kolsky) pressure bar apparatus used strain gauges to capture strain pulses. Due to space restrictions in the hutch, the load signal was measured with a load cell, instead of a typical transmission bar. Strain rates of roughly 1000 and 2000 s^{-1} were achieved.

For the synchrotron x-ray diffraction, multiple detector positions were selected from forward modelling with HiSPoD. The intent was to capture diffraction signals of interest from the BCC matrix β phase and orthorhombic α" martensite (space group No. 63, Cmcm) during microstructure evolution and mechanical testing. Since α" martensite is only a slight symmetry breakdown of the β phase, many of the diffraction peaks are either coincident with, or near the β phase reflections. The lower order symmetry of the orthorhombic space-group of the martensite also leads to additional reflections. Thoughtful selection of detector positions allowed for the measurement of the α" martensite reflections, without the overlap of β phase matrix reflections in some instances. Calibration measurements and diffraction forward modelling are further discussed in the Supplementary Materials.

4 Results

In the following sections, quasi-static, intermediate, and high strain rate mechanical testing and microstructure development in Ti-1023 are presented and discussed, including the role of aging.

4.1 Mechanical Data

4.1.1 Quasi-Static and Intermediate Strain Rates

The AQ, MTS and TI conditions were quasi-statically strained at 10^{-3} s^{-1}. The engineering stress/strain and true stress/strain curves are shown in Figure 1a–b, respectively. The engineering stress/strain curves show a clear trend in the effect of low-temperature aging on yield stress. Microstructural characterization of the AQ and aged conditions deformed at quasi-static strain rates is reported elsewhere [4]. Optical microscopy of the tensile specimens deformed at intermediate strain rates revealed a transformed microstructure consistent with those produced by quasi-static strain rates, but is not shown here for conciseness. The yield stress increases from below 200 MPa for the AQ condition to over 600 MPa for the MTS condition, representing a more than three-fold increase in strength. Unexpectedly, the MTS condition also appears to exhibit larger total elongation than the AQ condition (Table 2). The TI condition shows an increased yield strength (722 MPa) compared to the MTS condition (607 MPa), but also exhibits reduced elongation (0.34 for MTS versus 0.16 for TI). When true stress/strain is considered, trends in the work hardening rate (WHR) and uniform elongation become evident. Low temperature aging significantly reduced the maximum WHR exhibited, as shown by the inset in Figure 1b. Low temperature aging also resulted in increased uniform elongation (0.26) of the MTS condition compared to the AQ condition (0.19), as discussed in the Supplementary Materials.

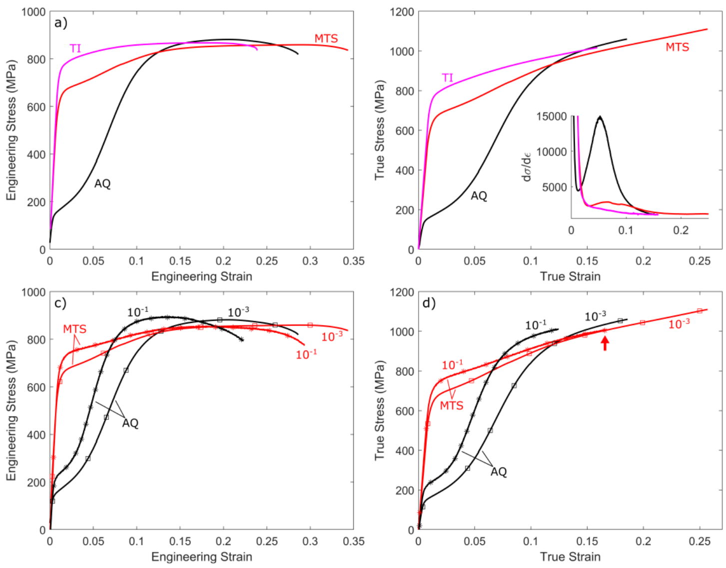

Figure 1: Quasi-static and intermediate strain rate mechanical response of Ti-1023 with aging. a) Engineering stress versus engineering strain and b) true stress versus true strain in the AQ, MTS and TI conditions. c) Engineering stress versus engineering strain curves for the AQ and MTS conditions tested at quasi-static (10^{-3} s^{-1}) and intermediate (10^{-1} s^{-1}) strain rates. d) True stress versus true strain curves for the AQ and MTS conditions tested at quasi-static and intermediate strain rates. The end of the intermediate strain rate MTS curve is indicated by a red arrow in d).

Quasi-static and intermediate strain rate testing was also performed on Ti-1023 in the AQ and MTS conditions to ascertain the effect of increasing strain rate on strengthening by low-temperature aging and TRIP. The AQ and MTS conditions were tested at a quasi-static strain rate of 10^{-3} s^{-1} and an intermediate strain rate of 10^{-1} s^{-1}. Engineering stress/strain and true stress/strain curves are shown in Figure 1c-d, respectively.

A hundred-fold increase in strain rate caused an increase in 0.2 % offset yield stress from 162 to 235 MPa for the AQ condition and 607 to 695 for the MTS condition. The increase in yield stress is accompanied by a decrease in uniform and total elongation for both the AQ and MTS conditions

(Table 2). On the other hand, both conditions exhibit decreasing Ultimate Tensile Stress (UTS) as strain rate increased from 10^{-3} to 10^{-1} s^{-1}. The UTS decreased from 1059 to 1007 MPa for the AQ condition and from 1110 to 1004 MPa for the MTS condition. The increase in yield stress and decrease in UTS with strain rate aligns with Ma *et al.*'s reported results [20]. Ma *et al.* also reported the initial yield stress exhibited a strong positive strain rate sensitivity (SRS), whereas the UTS exhibited a slightly negative SRS.

Table 2: Mechanical Properties from Quasi-static and (Intermediate) Strain Rates from the AQ, MTS and TI conditions.

	0.2 % Offset Yield Stress (MPa)		Ultimate Tensile Stress (MPa)		Uniform Elongation		Total Elongation	
$\dot{\varepsilon}$ (s^{-1}) / Condition	10^{-3}	10^{-1}	10^{-3}	10^{-1}	10^{-3}	10^{-1}	10^{-3}	10^{-1}
AQ	162	235	1059	1007	0.19	0.12	0.27	0.22
MTS	607	695	1110	1004	0.26	0.17	0.34	0.2
TI	722	N/A	1016	N/A	0.16	N/A	0.24	N/A

4.1.2 High Strain Rate Mechanical Data

The high strain rate (modified Kolsky) pressure bar setup used in this work allowed for determination of stress and strain responses during synchrotron x-ray imaging and diffraction. Figure 2 shows high strain rate mechanical testing results at 1000 or 2000 s^{-1} for the AQ, MTS and TI conditions. Individual test results are shown in grey, which were used to calculate average curves shown in black. The averaging was performed due to the high variability exhibited by the individual specimens for a given condition. The variability is likely caused by the size of the specimens relative to the grain size, varying texture within each specimen, and/or the use of a load cell instead of a transmission bar to measure the load signal.

Total ductility was determined using a cut-off stress for each condition to compare values, as the exact moment of fracture is nearly impossible to determine from these tests. Ductility decreases as strain rate increases for all aging conditions studied. The elongations decrease by 0.01, 0.05 and 0.04, as strain rate goes from 1000 to 2000 s^{-1}, for the AQ, MTS and TI conditions, respectively. Ductility also decreases as aging time increases at constant strain rate. The elongations are 0.20, 0.15 and 0.13 at 1000 s^{-1}, for the AQ, MTS and TI conditions, respectively. Average flow stress increases with aging time at constant strain rate, indicating that low temperature aging still provides a strengthening effect at high strain rates. The average maximum flow stresses are roughly 882, 1056 and 1110 MPa at 1000 s^{-1} for the AQ, MTS and TI, respectively. Increasing strength

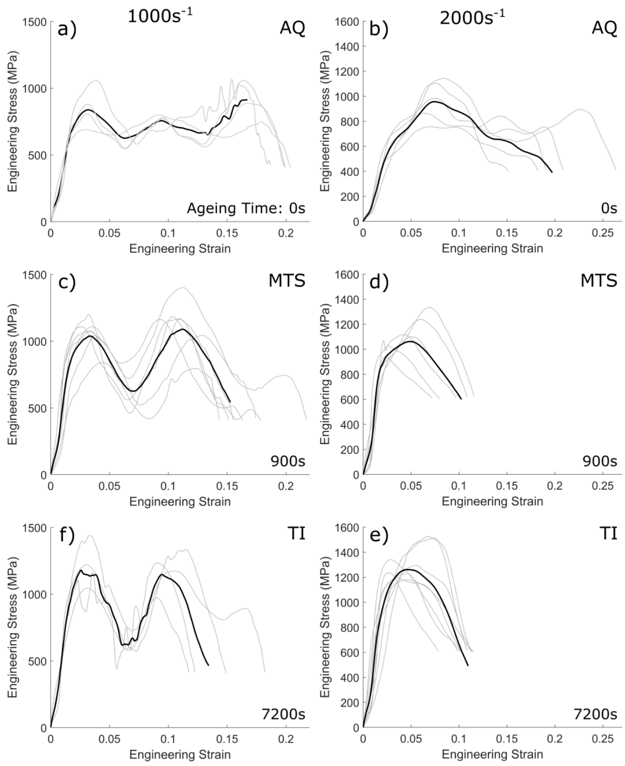

Figure 2: High strain rate mechanical testing results from (modified Kolsky) pressure bar testing during synchrotron x-ray imaging and diffraction. AQ specimens at a) 1000 s^{-1} and b) 2000 s^{-1}, MTS specimens at c) 1000 s^{-1} and d) 2000 s^{-1}, TI specimens at e) 1000 s^{-1} and f) 2000 s^{-1}. In all cases, individual specimen test results are shown in grey and average behavior for a given condition is shown in black.

with increasing strain rate is also exhibited for each aging condition. The average maximum flow stresses were roughly 956, 1061 and 1261 MPa at 2000 s^{-1} for the AQ, MTS and TI, respectively.

Pronounced signal oscillations are seen in the stress/strain response of all aged conditions at 1000 s^{-1}. These oscillations are absent from the 2000 s^{-1} tests, due to the shorter time to fracture. **The oscillations are likely due to ringing occurring in the specimen and load cell during the testing. Details of the testing setup and discussion associated can be found in the supplementary materials of Ellyson et al. [18].** The amplitude of the oscillations appears to be much lower for the AQ condition. The maximum average amplitude of the oscillations is 286 MPa for the AQ condition at 1000 s^{-1} compared to 413 and 540 MPa for the MTS and TI conditions at 1000 s^{-1}, respectively. Decreased ringing amplitude appears to indicate the AQ condition in Ti-1023 has a higher internal damping coefficient, which may help to explain the increased ductility exhibited by the AQ condition compared to the aged conditions.

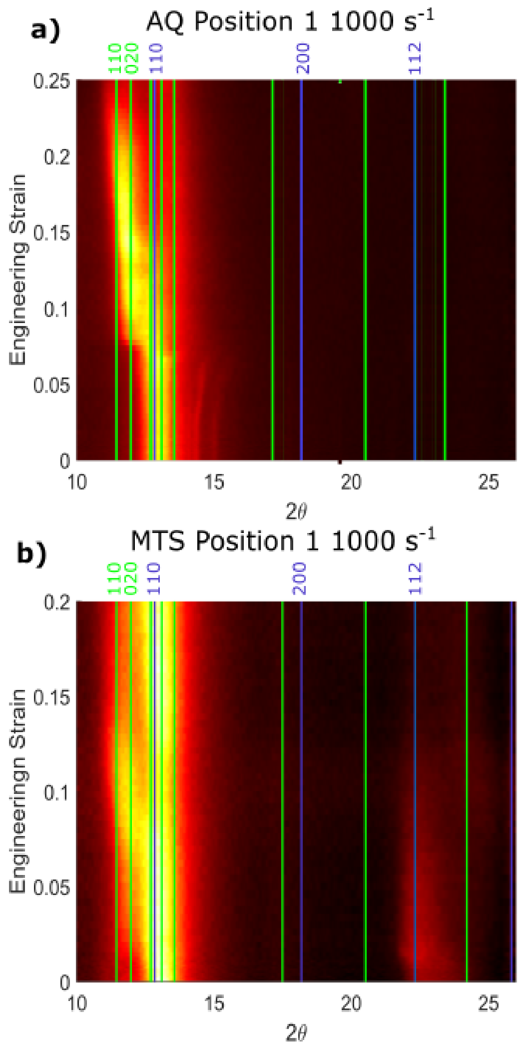

Figure 3: Integrated diffraction maps as a function of engineering strain for two specimens taken from detector position 1 (described in the Supplementary Materials) for a) an AQ specimen and b) and an MTS specimen. Both plots show stacked lineouts in the form of a heat map calculated by integrating individual frames and assembling them as a function of strain on the y axis. Theoretical diffraction positions for martensite (green), and beta phase (blue) are indicated with labeled reflections of interest for discussion purposes.

4.2 In-Situ Synchrotron X-Ray Diffraction during High Strain Rate Testing

In-situ synchrotron x-ray diffraction data taken from detector position 1 (described in the Supplementary Materials) provides the broadest range of d-spacings. Detector position 1 samples the highest intensity peaks for both the β phase and martensite, i.e. the $\{110\}_\beta$ and $\{111\}_{\alpha"}$ (Figure 10). Both peaks are nearly identical in d-spacing, as the $\{111\}_{\alpha"}$ planes are formed from the $\{110\}_\beta$ planes. In-situ data taken from detector position 1 leads to significant overlap of diffracted intensities, depending upon which peaks are measured and the initial texture present, as discussed in the Supplementary Materials. Figure 3a-b show two sets of stacked diffraction patterns as interpolated heat maps of 2θ versus engineering strain for both the MTS and AQ conditions, respectively.

Differences between the two conditions are visible for the theoretical positions of interest labeled in blue for β and green for α" above each of the heatmaps. For the MTS condition, intensity starts to appear near the $\{110\}_{\alpha"}$ and $\{020\}_{\alpha"}$ peaks almost immediately after yielding begins (near 0.02 strain), showing evidence for the onset of transformation. Maximum intensity is reached near 0.1 total strain and corresponds to the lowest intensity of the $\{110\}_{\beta}$ peak. The minimum β intensity coupled to a maximum in martensite intensity indicates that transformation has reached the maximum extent. This is strongly supported by the steady loss of intensity near the $\{112\}_{\beta}$ peak. From 0.1 total strain onward, the intensity at the $\{110\}_{\beta}$ peak increases at the expense of every other peak. The increase is indicative of texture evolution in both phases, most likely due to slip and internal twinning occurring from this strain up to fracture. It is impossible to determine to which degree each of the two phases is contributing to the measured intensity, due to broadening and overlap of the diffraction peaks. Intensity remains around the $\{110\}_{\alpha"}$ and $\{020\}_{\alpha"}$ up to the point of fracture, whereas diffraction from the secondary peaks of the β phase is mostly absent. This indicates the microstructure is composed mainly of martensite before fracture, and what little β phase remains is strongly textured.

A stacked diffraction heat map is shown for the AQ condition (Figure 3a). The onset of transformation occurs with yielding for the AQ condition, similar to the MTS condition. Conversely, in the AQ condition the degree of transformation increases faster as a function of plastic strain, since most of the diffracted intensity moves to the $\{110\}_{\alpha"}$ and $\{020\}_{\alpha"}$ peaks before 0.1 strain. Diffracted intensity at the $\{110\}_{\beta}$ position decreases rapidly, in conjunction with the increase in martensite diffracted intensity. The near total absence of β diffracted intensity implies that nearly complete transformation has occurred in this specimen as soon as 0.1 to 0.12 total strain. Interestingly, the relative intensity of the diffraction peaks exhibited by the AQ condition is completely different from that observed by the MTS condition throughout the test, as shown in Figure 3a-b. This is indicative of a different texture component evolving in the AQ condition compared to the MTS condition. However, the starting texture of each specimen is likely different, as discussed in the Supplementary Materials.

Detector position 2 (see Supplementary Materials) was used to track phase fraction evolution more precisely. The time-resolved diffraction obtained from detector position 2 allows for direct comparison of microstructural evolution with the mechanical testing data. Figure 4 shows integrated diffraction intensity for an AQ specimen. The diffraction peaks were integrated using +/- 0.5° range from the theoretical position. Figure 4 shows integrated intensity for the $\{112\}_{\beta}$, $\{132\}_{\alpha"}$ and $\{022\}_{\alpha"}$ peaks taken from position 2, along with engineering stress, both as a function of engineering strain. The data exhibits five distinct stages. In stage I, the onset of loading occurs as the stress pulse initially arrives at the specimen. In most tested specimens, the diffraction signal showed clear signs of specimen unbending at the onset of loading. The end of stage I also coincides with the onset of yielding and transformation. In stage II the intensity of the $\{112\}_\beta$ peak consistently decreases, and the integrated intensity of the $\{132\}_{\alpha''}$ and $\{022\}_{\alpha''}$ peaks increase in parallel. Interestingly, stage II also corresponds to a decrease in stress response, or strain softening. Stage III shows a distinct change in transformation behavior. The overall rate of transformation decreases, as can be seen by the lower rate of decrease in $\{112\}_\beta$ integrated intensity. Stage III is also accompanied by a change in relative intensity of the martensite reflections, which is indicative of texture evolution. Stage III appears to correspond to a slowdown in transformation, as the untransformed β phase is consumed and the capacity for further transformation is exhausted. Deformation via slip and twinning increase to compensate for the imposed plastic strain that transformation no longer accommodates. The gradual change in dominant deformation mechanisms is also accompanied by an increase in the stress response. The increasing stress indicates work hardening operating in both phases. Stage IV begins with a global reduction in total intensity of the diffraction data. The reduction in global intensity marks the onset of necking and fracture. Synchrotron x-ray imaging shows local thinning in the necked region (Figure 4b). The volume of illuminated material contributing to diffracted intensity is steadily decreasing, due to thinning of the necked region. Stage V corresponds to fracture, verified by the imaging data for this specimen (Figure 4c—d).

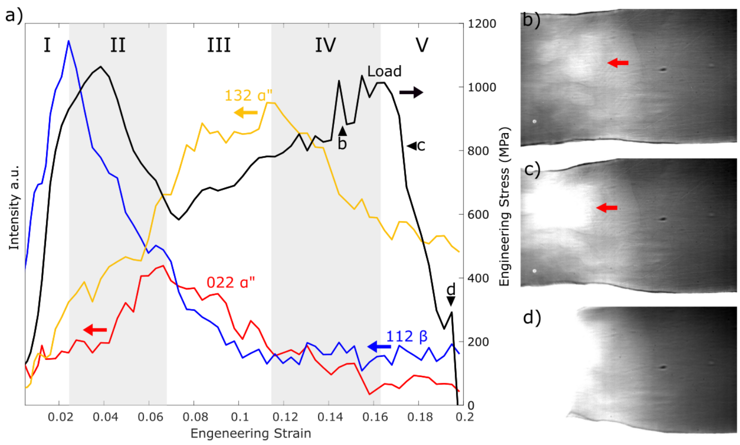

Figure 4: In-situ synchrotron x-ray imaging and diffraction of an AQ specimen deformed at 1000 s^{-1}. a) Integrated intensity from in-situ synchrotron x-ray diffraction and engineering stress as a function of engineering strain for an AQ specimen deformed at 1000 s^{-1}. Diffraction was taken at detector position 2. b) Synchrotron x-ray radiography taken near the UTS where the onset of local thinning is visible, as indicated by the red arrow. c) Synchrotron x-ray radiography taken after the UTS where fracture started, indicated by the red arrow. d) Synchrotron x-ray radiography taken after fracture, showing only the fixed end of the specimen.

Integrated intensity of diffraction peaks from the β and α" phases measured at detector position 2 and engineering stress versus engineering strain obtained from a MTS specimen is presented in the Supplementary Materials. As soon as the yield stress is reached, the integrated intensity of the $\{112\}_\beta$ peak starts decreasing and the $\{132\}_{\alpha"}$ peak correspondingly increases (Stage II). The $\{132\}_{\alpha"}$ reaches a maximum value near a strain of 0.09 (Stage III), at which point both peaks steadily decrease in intensity (Stage IV) until fracture occurs near 0.19 strain (Stage V). Overall, the results indicate that transformation slows down considerably and is nearly complete past 0.1 strain. Although the diffraction signal does not clearly show similar texture evolution in the martensite as that shown in Figure 4 since a single peak is measured, slip and twinning are most likely operating as the principal deformation mechanisms from 0.1 strain to fracture. Maximum stress is reached near 0.12 total strain, at which point necking initiates and the total diffracted intensity from both phases and the stress steadily decrease up to the point of fracture. In comparison to the behavior of the AQ specimen (Figure 4), stage III is much shorter for the MTS condition than the AQ condition.

The synchrotron x-ray diffraction data for the TI condition is harder to interpret than for the other two conditions. Transformation is not consistently detected in the diffraction signal, but was confirmed in certain specimens. These results are presented in the Supplementary Materials. As further confirmation, transformation was also discernible in the radiography for many of the specimens, including the TI condition. The synchrotron x-ray radiography results are not shown, but confirm the diffraction results.

4.3 Post-Mortem Microstructure Characterization

EBSD was conducted on the gauge section of the AQ, MTS, and TI specimens deformed at 1000 s^{-1}. Figure 5 shows an Inverse Pole Figure (IPF) + Image Quality (IQ) map in a) and a Phase + IQ map in b). Fine laths in multiple different orientations cover most of the scanned area. The original, equiaxed β phase grain boundaries are also visible. The IPF + IQ map shows a single subset of orientations hosted within a given grain. Most grains exhibit two or three common orientations of martensite. The common orientations suggest a strong tendency for variant selection, based on resolved shear stress. The microstructure evolution shown in Figure 5 supports that martensite transformation is an effective mechanism for accommodating plastic strain, even at high strain rates in metastable β Ti alloys. The Phase + IQ map indicates that most of the indexed area can be attributed to α" martensite. When the area fraction is averaged over many scans, the AQ condition exhibits an α" phase fraction of 0.91.

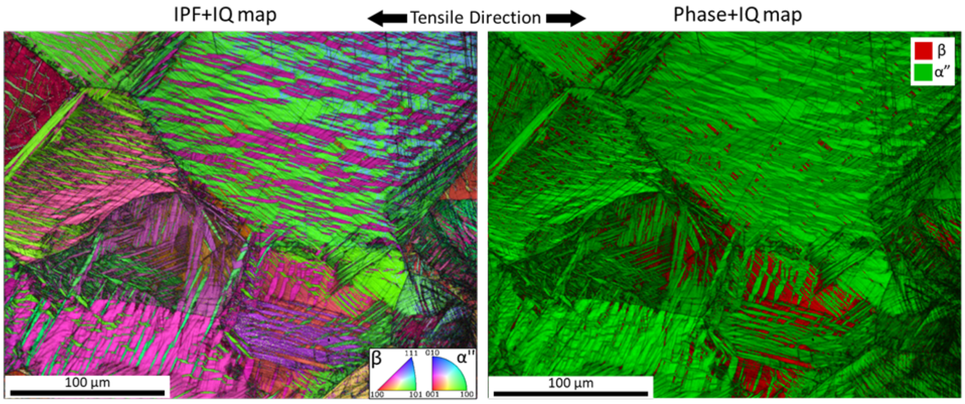

Figure 5: EBSD scan of an AQ specimen deformed at 1000 s^{-1}. a) IPF + IQ map and b) Phase + IQ map.

EBSD characterization was also performed on MTS specimens deformed at 1000 s^{-1}. Figure 6a-c show an IPF + IQ map, while b and d show the Phase + IQ maps of two different scans, respectively. The scan shown in 6c-d is a higher magnification scan of the area indicated by the yellow box in Figure 6a-b. Striking similarities are apparent between Figure 5 and parts of Figure 6a-b. Figure 6a shows a dense array of martensite laths populating prior β grains. The grain labeled "Grain A" in the Phase + IQ map in Figure 6b shows martensite laths of comparable width. Grain A has almost completely transformed to martensite, as evidenced by the densely packed laths, lack of misorientation across lath boundaries, and absence of measurable β phase in between.

Grain B, shown at high magnification in Figure 6c-d, reveals apparent difference in microstructure evolution and degree of transformation. Such grains were readily visible in many of the MTS specimens characterized by EBSD, much more so than in the AQ condition. The Phase + IQ map shows a lower degree of transformation in Grain B compared to Grain A, with the area fraction of martensite only 0.65 in Grain B compared to the more than 0.9 exhibited in Grain A.

The MTS condition appears to exhibit a higher proportion of partially transformed grains (e.g., Grain B) over completely transformed grains (e.g., Grain A) compared to the AQ condition. When the martensite area fraction is averaged over all areas characterized by EBSD for the MTS condition, the average area fraction is 0.77. The lower overall phase fraction of martensite is likely due to grains exhibiting nearly complete transformation (Grain A) with an area fraction near or exceeding 0.9 and grains that retain a significant portion of β phase (Grain B), where the local area fraction is usually near 0.6.

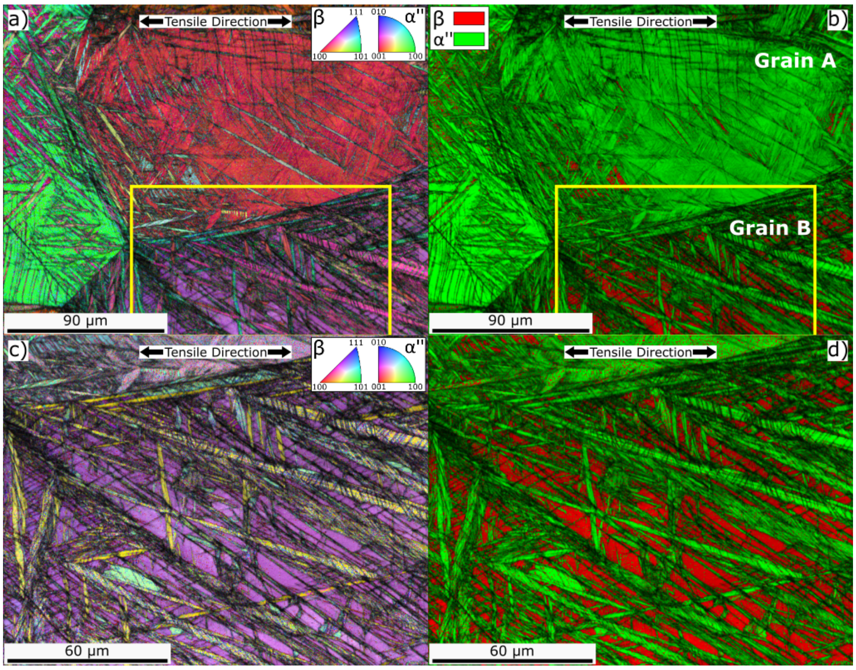

Figure 6: EBSD scan of an MTS specimen deformed at 1000 s^{-1}. a) IPF + IQ map and b) Phase + IQ map. c) IPF + IQ map and d) Phase + IQ map of the area highlighted in yellow in a) and b). This scan was taken from the same specimen shown in Figure 3a. Note the lower portion of the scan shown in c) and d) is outside the scan area shown in a) and b).

The average area fraction of martensite in the TI condition after fracture is the lowest of all three conditions studied for a given strain rate. EBSD scans of the gauge section of TI specimens deformed at 1000 s^{-1} (7) show partially transformed grains, more akin to Grain B shown in Figure 6. Fully transformed grains, like Grain A, were uncommon. Most grains contained an area fraction of martensite between 0.5 and 0.8. The IQ maps show signs of internal evolution within the primary martensite bands, likely from mechanical twinning of the transformation product. The heavy twinning of the martensite indicates plasticity continued after the primary martensite bands formed.

Post-mortem characterization of the TI condition also revealed a higher fraction of transformation occurred in the necked region compared to the gauge length. Microstructural evolution was the greatest in the necked region for all conditions, but the difference is the most striking for the TI condition. The TI aging treatment increases the stress necessary for transformation to a level comparable to or greater than the stress necessary for slip; however, the increased local strain rate and stress in the necked region leads to increased localized transformation. The localized transformation contributes to increasing post-uniform elongation, instead of uniform elongation.

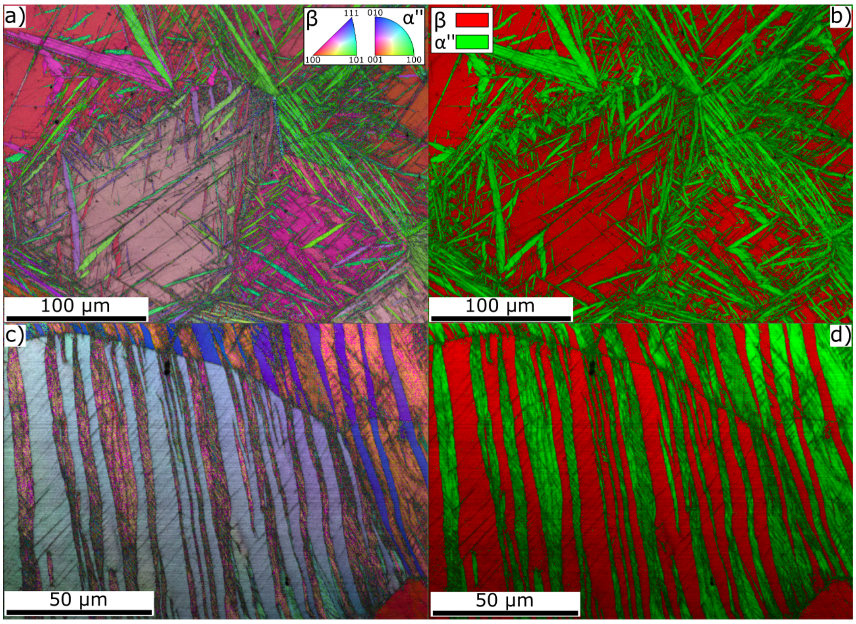

Figure 7: EBSD scan of two TI specimens deformed in tension at 1000 s^{-1}. a) IPF + IQ map and b) Phase + IQ map c) IPF + IQ map and (d) Phase + IQ map of another TI specimen. Both exhibit transformation, but at a lower phase fraction than observed for the AQ and MTS conditions.

5 Discussion

5.1 Low Temperature Aging and Transformation at High-Rates

Post-mortem characterization by EBSD was used to measure the area fraction of martensite in fractured specimens for each aged condition at both tested strain rates. The area fraction measurements were obtained from multiple scans performed on at least three samples per condition, per strain rate. More than 1 mm^2 of total scanned area was used to determine the average and standard deviation of the area fraction (Table 3). Increasing aging time caused a decrease in area fraction of martensite tested at both strain rates. The standard deviation of the mean area fraction also increases with aging time. **It should be noted that Ti-1023, as well as other TRIP and TRIP/TWIP β Ti alloys, have been reported, by means of in-situ tensile testing, to undergo some martensite reversion upon unloading, such that the unloaded state might not be perfectly representative of the microstructural state at the ultimate tensile stress.**

Table 3: Average area fraction (and standard deviation) of martensite for each condition and strain rate.

Condition	1000 s^{-1}	2000 s^{-1}
AQ	0.91 (0.03)	0.79 (0.09)
MTS	0.77 (0.11)	0.68 (0.09)
TI	0.63 (0.14)	0.55 (0.18)

While in-situ synchrotron x-ray diffraction shows an equivalence in the strain at which transformation initiates and slows for all conditions investigated, EBSD characterization shows the total area fraction of martensite decreases with increasing aging time (Table 3). As such, increasing aging time ultimately affects the total capacity for transformation at high strain rates, rather than the plastic strain over which transformation occurs.

Both Yang *et al.* [9] and Xiao *et al.* [10] tested TRIP/TWIP β Ti alloys at high strain rates in compression. Yang *et al.* tested TRIP/TWIP Ti-8.5Cr-1.5Sn (wt.%) at 1000, 1500 and 2000 s^{-1}. They found significant transformation and twinning in the deformed microstructure, with no apparent suppression of TRIP or TWIP, which corroborates well with the findings presented here. Xiao *et al.* conducted dynamic compression of TRIP/TWIP Ti-2Al-9.2Mo-2Fe (wt.%) at 3000 s^{-1}. Their study serves as an interesting comparison to these results, as they studied two microstructural conditions containing different ω phase populations produced by different solution treatment temperatures, followed by a quench to room temperature. The low-temperature condition (850 $°C$ for 30 min) contained small "un-evolved" ω phase precipitates, while the higher temperature condition (950 $°C$ for 60 min) contained larger, well-defined ellipsoidal ω phase precipitates after quenching. They found evidence of TWIP and TRIP at 0.1 and 0.17 true strain during testing in the low temperature condition, while they found only TWIP and no evidence of TRIP in the high temperature condition at the same true strain levels. All of their tests were conducted at high strain rate and room temperature. These results strongly support the present findings that athermal ω phase controls the propensity for TRIP at high strain rates (up to 2000 s^{-1} here and 3000 s^{-1} in Xiao *et al.*'s study). Secondly, it was also reported that microstructural evolution severely slowed after 0.1 true strain, with dislocation slip operating instead from 0.1 to 0.17 true strain.

Typically, no more than 5 to 10 grains were included in an area scanned with EBSD in this work. When the amount of transformation is reduced (as is the case with increasing aging time), the degree of transformation becomes more variable on a per grain basis. The increased variability supports the hypothesis that certain grains undergo significant transformation, whereas other grains transform less or by slip instead, effectively producing the "bi-modal" distribution of area fraction transformed exhibited by the MTS conditions (e.g., Grains A and B in Figure 6). This grain-by-grain selection of transformation or slip is most likely driven by the resolved shear stress on specific slip or transformation systems as a function of grain misorientation relative to the tensile axis, usually represented by the Schmid factor. Schmid factor analysis was performed on

EBSD maps reconstructed to contain only the parent β grains before deformation. Figure 8 shows a grain-by-grain Schmid factor map for the same EBSD scan shown in Figure 5. The grains in the lower sections of the scan in Figure 8 clearly show that the Schmid factor for slip is higher than that for transformation, while the phase map shown in Figure 5 proves the grains are almost fully transformed. This analysis supports the claim that, in the AQ condition, the stress for transformation is significantly lower than that for slip, which leads grains to transform even when unfavorably oriented relative to slip and leads to high area fraction of transformed material.

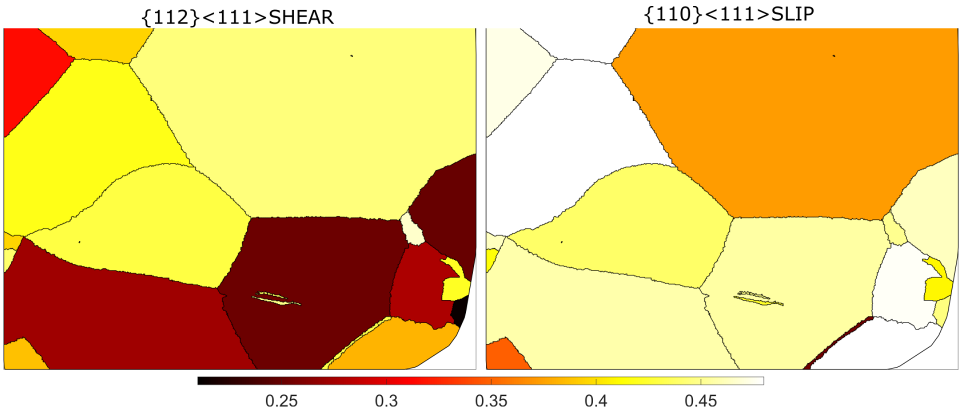

Figure 8: Schmid factor map for the reconstructed β phase obtained from an EBSD scan of an AQ specimen deformed at 1000 s^{-1} a) Schmid factor map for the martensitic transformation system b) Schmid factor map for the main BCC slip system. Note the bottom right corner of the map was unable to be reconstructed due to excessive deformation and was removed during the calculation process.

However, increasing aging time causes a gradual reduction of fully transformed grains (Grain A type), in favor of partially transformed grains (Grain B type), when deformed at high strain rates. This reduction in fully transformed grains is most likely due to an increase in transformation stress caused by increased aging. The increase in occurrence of partially transformed grains over fully transformed ones ultimately reduces the total area fraction of transformation product, as measured by EBSD, which directly correlates to reduced total elongation at both strain rates tested, i.e., 1000 s^{-1} and 2000 s^{-1} (Figure 9 b)).

In other words, if the stress for transformation is low, as is the case for the AQ condition, it is likely a larger portion of grains will reach the transformation stress of at least one variant before other deformation mechanisms (e.g., slip) activate from hardening (as shown in Figure 8). On the other hand, if the stress for transformation is comparable or greater than the stress for slip in the β phase, then some grains will deform by slip rather than transformation, or as a combination of both. This likely occurs to some extent in the MTS and TI conditions. The propensity for selecting a deformation mechanism other than phase transformation seems to increase with increasing strain rate. Since the microstructure is initially BCC, the stress for dislocation motion is strongly strain rate dependent, meaning that the β phase will reach a higher elastic stress before initiating slip at higher strain rates. Under these conditions, transformation is potentially favored if the stress for transformation is less strain rate sensitive than the stress for slip.

This conclusion is strengthened when quasi-static and intermediate strain rates are considered. Microstructural characterization for the quasi-static testing is presented in detail in a previous publication [4], while microstructural characterization for the intermediate strain rate tests are presented in the supplementary materials (Figure 16). In both cases, deformed material from interrupted tensile tests is presented. Ellyson et al. show that the degree of transformation does not differ strongly between aging condition during quasi-static deformation of samples deformed to 0.005 (0.5%) plastic strain by EBSD. Figure 16 shows micrographs taken from the gage section of intermediate strain rate specimens strained to 0.03 plastic strain. The AQ specimens exhibit a degree of transformation that is significantly higher than the MTS specimens. In fact, most of the microstructure of the MTS presents partially transformed grains, as compared to the high degree of transformation seen in the AQ specimen. It appears as though, as strain rate is increased, the rate at which transformation occurs as a function of plastic strain is reduced and that this trend increases for increased aging time. In other words, aging and strain rate have a strong interaction and individual effect in reducing the propensity for transformation during deformation. On the other hand, microstructural characterization hasn't revealed any significant difference in martensite morphology between aged conditions and strain rates. It should be mentioned, that the contrast seen on EBSD IQ maps does suggest that the internal structure of the martensite laths does become more complex as strain rate and aging increases, although fine scale characterization would be required to conclusively answer this question.

Ultimately, these results show the increased propensity for transformation (i.e., low stress for transformation) is beneficial for maintaining elongation at high strain rates in TRIP Ti alloys, as shown for the AQ condition. This key insight establishes a tradeoff between high strength at quasi-static strain rates and maintaining high elongation at strain rates up to 2000 s^{-1} when tuning the transformation stress in TRIP Ti alloys by low temperature aging.

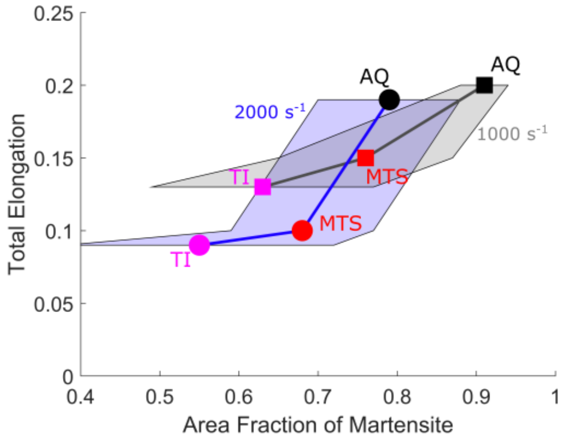

Figure 9: Effect of low temperature aging on the degree of phase transformation (i.e., TRIP) during high strain rate deformation. Total elongation versus area fraction of martensite for both strain rates (1000 s^{-1} and 2000 s^{-1}) tested. The shaded areas represent the variability in measured area fraction of martensite with EBSD. Aging conditions are indicated for each point in b).

5.2 Change in Strain Rate Sensitivity with Aging

An interesting finding from the high strain rate mechanical testing results is the reduced ringing amplitude exhibited by the AQ state at 1000 s^{-1}. Kolsky bars, or more generally pressure bars, use an elastic impulse travelling down an incident bar to load the specimen. Any mechanical oscillator submitted to a sudden acceleration will produce forced vibrations in response. Differences in ringing amplitude should be attributable to changes in internal damping coefficient. It then stands to reason that the reduced amplitude of the ringing exhibited by the AQ condition is likely due to an increased damping effect. A high internal damping subsequently reduced by low temperature aging would help to explain the decreased elongation observed with increasing aging time during high strain rate deformation of TRIP Ti-1023.

There is close conceptual connection between internal damping and strain rate sensitivity, m. Strain rate sensitivity is an important parameter in determining the ability of a material to delay instability and maintain uniform elongation. A strain rate sensitivity of 1 implies a material can undergo stable necking. The equivalency makes intuitive sense, since a high damping coefficient leads to a local stress increase in proportion to any localized increase in deformation speed, thus making these areas locally stronger and forcing de-localization of the deformation. If the AQ condition possess a higher strain rate sensitivity, it would allow for an increased resistance to necking and localization compared to conditions having undergone increased aging.

This hypothesis is further supported by the increased ductility exhibited by the AQ condition at strain rates of 1000 and 2000 s^{-1}. When strain rate is increased from 1000 to 2000 s^{-1}, the

AQ condition undergoes the greatest increase in average flow stress with the smallest decrease in total elongation compared to the aged conditions. Further testing is planned to examine the effect of low temperature aging on strain rate sensitivity. If confirmed, it would have implications for controlling the ω phase and low-temperature aging to modify the strain rate sensitivity of TRIP Ti alloys, while simultaneously optimizing for strength and ductility.

6 Conclusion

In this study, in-situ synchrotron x-ray diffraction was used to study microstructure evolution and phase transformation in aged Ti-1023 during high strain rate deformation. The AQ and two aged conditions were tested at quasi-static and intermediate strain rates of 10^{-3} and 10^{-1} s^{-1}, respectively, and compared to testing performed at 1000 and 2000 s^{-1}. In-situ synchrotron x-ray diffraction and EBSD were used to examine the transformation product. The following conclusions can be drawn from the present work:

- High strain rate mechanical testing indicates the strengthening provided by low-temperature aging (and the ω phase) is retained at strain rates up to 2000 s^{-1} .
- Quasi-static (10^{-3} s^{-1}) and intermediate (10^{-1} s^{-1}) strain rate testing in conjunction with high strain rate tensile data confirm that ductility decreases as strain rate increases over 6 orders of magnitude for all conditions.
- In-situ synchrotron x-ray diffraction shows phase transformation and the TRIP effect is the most active from yielding to ∼0.1 strain. The plastic strain range over which transformation occurs during high strain rate testing is not strongly affected by low-temperature aging. Low-temperature aging reduces the total transformed fraction of martensite.
- Post-mortem EBSD reveals the total fraction of phase transformation decreases significantly with increasing aging time at high strain rates. The area fraction of transformed martensite falls from 0.91 in the AQ condition to 0.76 and 0.63 in the MTS and TI conditions, respectively, for strain rates of 1000 s^{-1}.
- Post-mortem microstructure characterization of samples tested at high strain rates reveals the area fraction of martensite varies strongly on a per grain basis for the MTS and TI conditions, while the AQ condition exhibits nearly complete transformation throughout the microstructure. The decrease in occurrence of fully transformed grains (Grain A in 6) in favor of partially transformed grains (Grain B in 6) as aging increases leads to a global reduction

in area fraction of transformation product. The reduction in transformation correlates to a reduced total elongation at strain rates of 1000 and 2000 s^{-1} (Figure 9 b).

The findings presented in this work have important implications for the future design of TRIP-capable microstructures in metastable β Ti alloys. The ω phase and low temperature aging have a direct impact on ductility at high strain rates via the extent of transformation during deformation.

7 Aknowledgements

This work was supported by the department of the Navy, Office of Naval Research under award No. N00014-18-1-2567. Any opinions, findings, and conclusions or recommendations expressed in this material are those of the author(s) and do not necessarily reflect the views of the Office of Naval research. The authors gratefully acknowledge ATI (Allegheny Technologies Incorporated) for providing the Ti-1023 studied in this work. The authors also thank the Center for Advanced Non-Ferrous Structural Alloys (CANFSA), a National Science Foundation Industry/University Cooperative Research Center (I/UCRC) [Award No. 2137243] at the Colorado School of Mines for support during the preparation of this manuscript. This research used resources of the Advanced Photon Source, a US Department of Energy (DOE) Office of Science User Facility operated for the Office of Science by Argonne National Laboratory under contract no. DE-AC02-06CH11357.

8 Declaration of Competing Interests

The authors have no competing interests to declare.

References

[1] Donachie MJ. Titanium: a technical guide. ASM international; 2000.

[2] Montgomery JS, Wells MG. Titanium armor applications in combat vehicles. JOM. 2001;53(4):29–32.

[3] Matlock DK, Speer JG, De Moor E, Gibbs PJ. Recent developments in advanced high strength sheet steels for automotive applications: an overview. Jestech. 2012;15(1):1–12.

[4] Ellyson B, Klemm-Toole J, Clarke K, Field R, Kaufman M, Clarke A. Tuning the strength and ductility balance of a TRIP titanium alloy. Scripta Materialia. 2021;194:113641.

[5] Duerig T, Terlinde G, Williams J. Phase transformations and tensile properties of Ti-10V-2Fe-3AI. Metallurgical Transactions A. 1980;11(12):1987–1998.

[6] Sun F, Zhang J, Vermaut P, Choudhuri D, Alam T, Mantri S, et al. Strengthening strategy for a ductile metastable β-titanium alloy using low-temperature aging. Materials Research Letters. 2017;5(8):547–553.

[7] Danard Y, Poulain R, Garcia M, Guillou R, Thiaudière D, Mantri S, et al. Microstructure Design and in-situ investigation of TRIP/TWIP effects in a forged dual-phase Ti–10V–2Fe–3Al alloy. Materialia. 2019:100507.

[8] Ahmed M, Wexler D, Casillas G, Savvakin DG, Pereloma EV. Strain rate dependence of deformation-induced transformation and twinning in a metastable titanium alloy. Acta Materialia. 2016;104:190–200.

[9] Yang H, Wang D, Zhu X, Fan Q. Dynamic compression-induced twins and martensite and their combined effects on the adiabatic shear behavior in a Ti-8.5 Cr-1.5 Sn alloy. Materials Science and Engineering: A. 2019;759:203–209.

[10] Xiao J, Nie Z, Tan C, Zhou G, Chen R, Li M, et al. The dynamic response of the metastable β titanium alloy Ti-2Al-9.2 Mo-2Fe at ambient temperature. Materials Science and Engineering: A. 2019;751:191–200.

[11] Standard A. E8. Standard test method for tension testing of metallic materials. West Conshohocken (USA): ASTM. 2004.

[12] Bachmann F, Hielscher R, Schaeben H. Texture Analysis with MTEX – Free and Open Source Software Toolbox;160:63–68. Available from: https://www.scientific.net/SSP.160.63.

[13] Niessen F, Nyyssönen T, Gazder AA, Hielscher R. Parent grain reconstruction from partially or fully transformed microstructures in MTEX. Available from: http://arxiv.org/abs/2104.14603.

[14] Duerig TW, Middleton RM, Terlinde GT, Williams JC. Stress Assisted Transformation In Ti-10V-2Fe-3Al;2.

[15] Wang Y, Liu X, Im KS, Lee WK, Wang J, Fezzaa K, et al. Ultrafast X-ray study of dense-liquid-jet flow dynamics using structure-tracking velocimetry. Nature Physics. 2008;4(4):305–309.

[16] Hudspeth M, Claus B, Dubelman S, Black J, Mondal A, Parab N, et al. High speed synchrotron x-ray phase contrast imaging of dynamic material response to split Hopkinson bar loading. Review of Scientific Instruments. 2013;84(2):025102.

[17] Hudspeth M, Sun T, Parab N, Guo Z, Fezzaa K, Luo S, et al. Simultaneous X-ray diffraction and phase-contrast imaging for investigating material deformation mechanisms during high-rate loading. Journal of Synchrotron Radiation. 2015 Jan;22(1):49–58.

[18] Ellyson B, Fezzaa K, Sun T, Parab N, Saville A, Finfrock C, et al. Transformation and twinning induced plasticity in metastable Ti-Mo alloys under high strain rate deformation. Materials Science and Engineering: A. 2022:143716.

[19] Sun T, Fezzaa K. HiSPoD: a program for high-speed polychromatic X-ray diffraction experiments and data analysis on polycrystalline samples. Journal of synchrotron radiation. 2016;23(4):1046–1053.

[20] Ma X, Li F, Cao J, Li J, Sun Z, Zhu G, et al. Strain rate effects on tensile deformation behaviors of Ti-10V-2Fe-3Al alloy undergoing stress-induced martensitic transformation. Materials Science and Engineering: A. 2018;710:1–9.

9 Supplementary Discussion

9.1 Synchrotron X-ray Detector Calibration

HiSPoD was used to model the resulting diffraction patterns from both detector positions to confirm that martensite could be successfully detected (Figure 10a–b). Crystallographic data used is presented in Table 5 The first detector position (10a) was selected to measure the most intense peaks from both the parent and product phases, which include the $\{110\}_{beta}$ and $\{111\}_{\alpha"}$ near 13°. Examples of lattice correspondence for specific families of planes are shown in Table 4. The second detector position (Figure 10b) was selected to more carefully measure changes in relative phase fraction, as two peaks from each phase are found in this position: ($\{112\}_{\beta}$ and $\{200\}_{\beta}$) and ($\{132\}_{\alpha"}$ and $\{022\}_{\alpha"}$). This detector position also avoids intensity wash-out from the higher intensity and overlapping peaks at lower 2θ positions. The difference in relative intensity can be seen in the right-most portion of Figure 10a compared to Figure 10b.

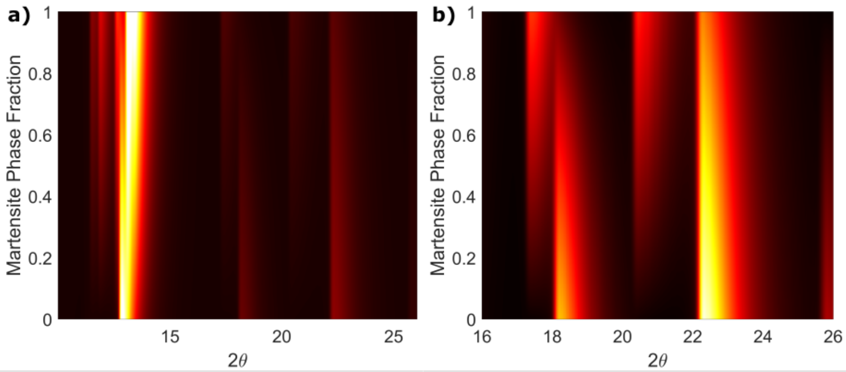

Figure 10: Simulated integrated diffraction patterns for Ti-1023 as a function of martensite phase fraction for detector a) position 1 and b) position 2.

Figure 11 shows simulated and measured diffraction patterns obtained from the high-purity Ta foil. Full rings of diffraction intensity were obtained due to the fine grain size of the Ta foil, which aided in detector position calibration. The simulated patterns (Figure 11a–b) were obtained from HiSPoD and consider only broadening occurring from the energy spectrum of the incident beam.

Table 4: Crystallographic correspondence for symmetry related martensitic variants for specific matrix planes

Variants	g=$\{110\}_{\beta}$	g=$\{112\}_{\beta}$
V1	g=$\{11\bar{1}\}_{\alpha"}$	g=$\{131\}_{\alpha"}$
V2	g=$\{111\}_{\alpha"}$	g=$\{1\bar{1}3\}_{\alpha"}$
V3	g=$\{\bar{1}11\}_{\alpha"}$	g=$\{13\bar{1}\}_{\alpha"}$
V4	g=$\{1\bar{1}1\}_{\alpha"}$	g=$\{113\}_{\alpha"}$
V5	g=$\{020\}_{\alpha"}$	g=$\{220\}_{\alpha"}$
V6	g=$\{002\}_{\alpha"}$	g=$\{202\}_{\alpha"}$

Table 5: Crystallographic information used for Ti-1023

Phase	Space Group	Lattice Parameters (Å)	Atom Position
β	229	a=3.327	(0 0 0)
α”	63	a=3.01 b=4.91 c=4.63	(0 0.185 0.25)

The broad, asymmetric profile of the “pink-beam" energy spectrum is evident in the broadening of the rings of the simulated Ta pattern (e.g. $\{110\}_\beta$ ring in Figure 11a). When the measured patterns (Figure 11c–d) are compared with simulated patterns, other sources of peak broadening become apparent. These sources include, but are not limited to, beam size, scattering from air, and microstructural parameters such as residual stress or grain size. The most prominent factors contributing to broadening remain, nonetheless, the energy spectrum and the beam size. The comparison of simulated and measured diffraction rings of the Ta foil and the relative broadening exhibited are crucial factors to consider when experimental diffraction results are presented in this work.

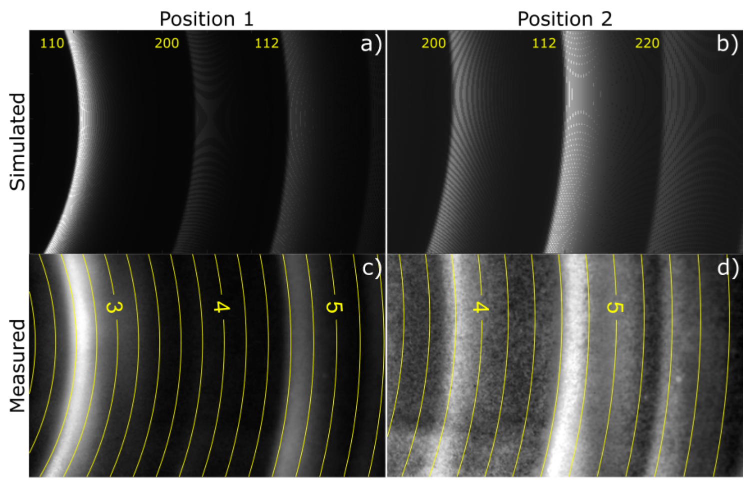

Figure 11: a-b) Simulated and c-d) measured raw diffraction patterns of Ta foil for both detector positions used. Simulated powder patterns obtained from HiSPoD for a) detector position 1 and b) detector position 2. The diffraction rings are labeled in yellow. Measured diffraction patterns for fine-grained Ta foil corresponding to c) position 1 and d) position 2. The yellow circular arcs represent lines of constant q (nm^{-1}) with positions for 3, 4 and 5 nm^{-1} labeled. The simulated pattern considers only broadening from the synchrotron x-ray energy spectrum. Other sources of experimental broadening are apparent in the measured patterns.

9.2 Initial Texture of Tensile Specimens

The as-received Ti-1023 was 50.8 mm diameter round bar with a radially symmetric rolling texture across the cross-section. Rectangular blocks were extracted from the round bar to serve as blanks for the miniature tensile specimens. The miniature tensile specimens were extracted by conventional machining in the same orientation of the rectangular blocks. The orientation of the rectangular blocks and tensile specimens was chosen so the tensile axis was aligned with the rolling direction. The axisymmetric nature of the rolling texture ensures that the texture component along the tensile direction is the same for all specimens. The way in which the texture component differed was in the transverse direction (Figure 12). If the broad, flat face of a tensile specimen is taken as the reference direction, two limiting cases emerge. First, when the specimen is extracted with the flat face parallel to the radial direction (i.e., the bottom or top of the bar cross-section). Second, when the specimen is extracted with the flat face parallel to the tangential direction of the bar (i.e., the sides of the bar cross-section). The extraction strategy caused a distribution of initial texture components in the transverse and normal directions. Since the specimens were randomized when they were associated to a given aging condition and a total of nearly 60 specimens were tested, the texture distribution is averaged for the overall trends, such as mechanical properties. The variability in initial texture becomes important when individual specimens are compared across aging conditions. As such, every effort was made to consider this discrepancy when discussing texture evolution from the in-situ diffraction data.

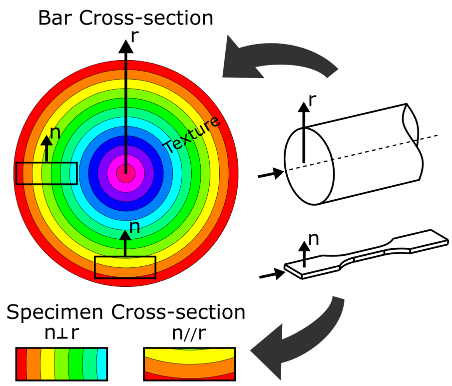

Figure 12: Schematic of the texture component of miniature specimens stemming from the chosen extraction strategy from initial round bar stock. The schematic indicates how the radially symmetric texture leads to different texture components in flat specimens.

9.3 Grain Size Effects and Low-Temperature Aging

Quasi-static strain rate mechanical testing data presented here appears to show a different trend in low temperature aging response compared to previously reported results [4]. This is most likely attributable to differences in grain size in the initial material, as the alloy composition is the same. Grain size effects and the interaction with low-temperature aging on TRIP in Ti alloys has been unreported in the literature. In light of this, a short discussion is warranted. Substantial post-uniform elongation is exhibited by all three conditions in the quasi-static and intermediate strain rate engineering stress/strain response (Figure 1a). Increased post-uniform elongation contrasts with previous results, where post-uniform elongation was negligible in the AQ and MTS conditions, as coarser grained material was investigated (250 μm average grain size) [4]. Additionally, the TI condition in this work is found to exhibit some transformation. This is in stark contrast with the TI condition reported previously, where transformation was completely absent and deformation was characterized by localized slip bands. This indicates the onset of TRIP inhibition and, more broadly, the aging response is affected by grain size, as both conditions were aged for 7200 s at 423 K. The stock used in this study has a grain size roughly 3x smaller than that used previously. The chemical composition in both studies is nominally the same (specifically oxygen content). The effect of grain size on low temperature aging is outside the scope of this work, but will be explored in an upcoming publication.

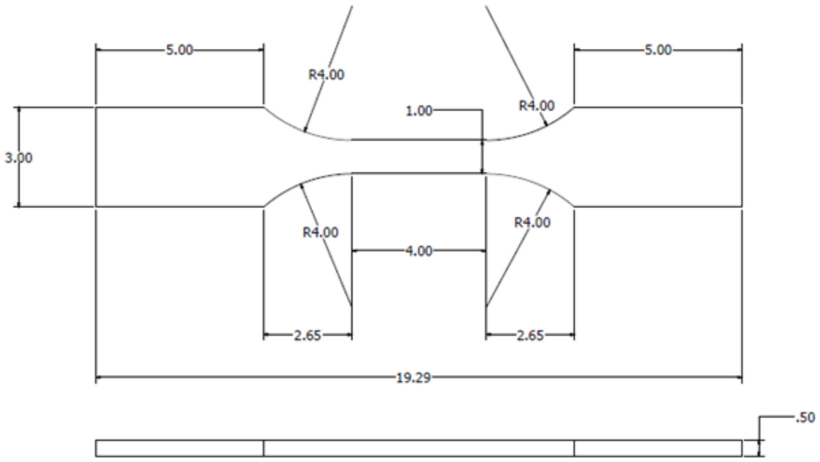

Figure 13: Geometry of the miniature tensile specimens used for the in-situ high strain rate testing at the Advanced Photon Source at Argonne National Laboratory.

Figure 14b shows the integrated diffraction heatmap as a function of engineering strain from a TI specimen, exhibiting clear signs of transformation. The integrated diffraction heatmap (Figure 14b) is presented on the same x-axis as the engineering stress/strain curve (Figure 14a). The decrease in β phase fraction caused by the onset of transformation can be seen to start around 0.01 strain, or the same strain as the onset of yielding (stage II). Additionally, the diffraction shows a decrease in diffracted intensity of the β phase near 0.1 total strain (Figure 14b). This decrease in β diffracted intensity corresponds to the maximum stress being reached in the stress/strain curve (Figure 14a). The decrease in diffracted intensity comes from necking and the decrease in illuminated volume (stage IV), as confirmed by the x-ray imaging. Raw diffraction frames are presented in Figure 14c-d, where a large single reflection near the theoretical β diffraction position (Figure 14c) splits into two distinct spots just after yielding (Figure 14d). The diffraction frames show the evolution of a single grain transformed into many smaller martensite laths in residual β

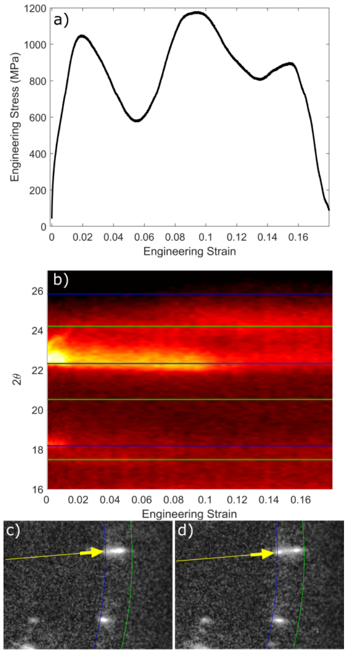

Figure 14: In-situ mechanical testing and synchrotron x-ray diffraction data for a TI specimen deformed in tension at 1000 s^{-1}. a) Engineering stress versus engineering strain curves. b) An integrated diffraction heatmap of 2θ versus engineering strain with theoretical positions of peaks for both phases overlaid (yellow corresponds to β and green corresponds to α"). c) Raw diffraction frame just before the onset of loading. d) Raw diffraction frame just after yielding. In both c) and d) the yellow arrow highlights the reflections of interest, which is the $\{112\}_{\beta}$ and the $\{132\}_{\alpha"}$, the line indicates the radial direction from the beam position, while the blue and green arcs represent the theoretical position of a β phase and martensite diffraction rings, respectively.

phase, since both reflections become smaller, move in tandem, and are always on the same radial line (yellow line in Figure 14c-d). In most TI specimens, it appears as though relative intensity and peak overlap contribute to washing-out the diffracted intensity from the martensite.

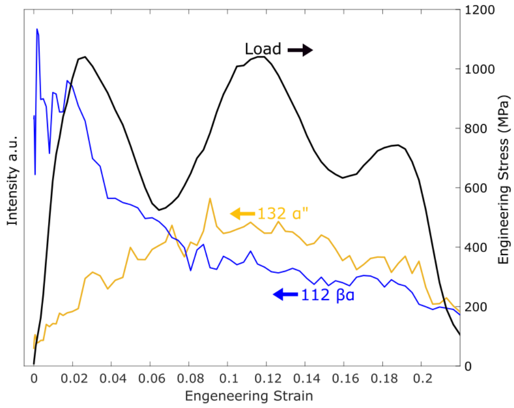

Figure 15: Integrated intensity from synchrotron x-ray diffraction and engineering stress as a function of engineering strain for an MTS specimen deformed at 1000 s^{-1}. Diffraction data was taken in detector position 2.

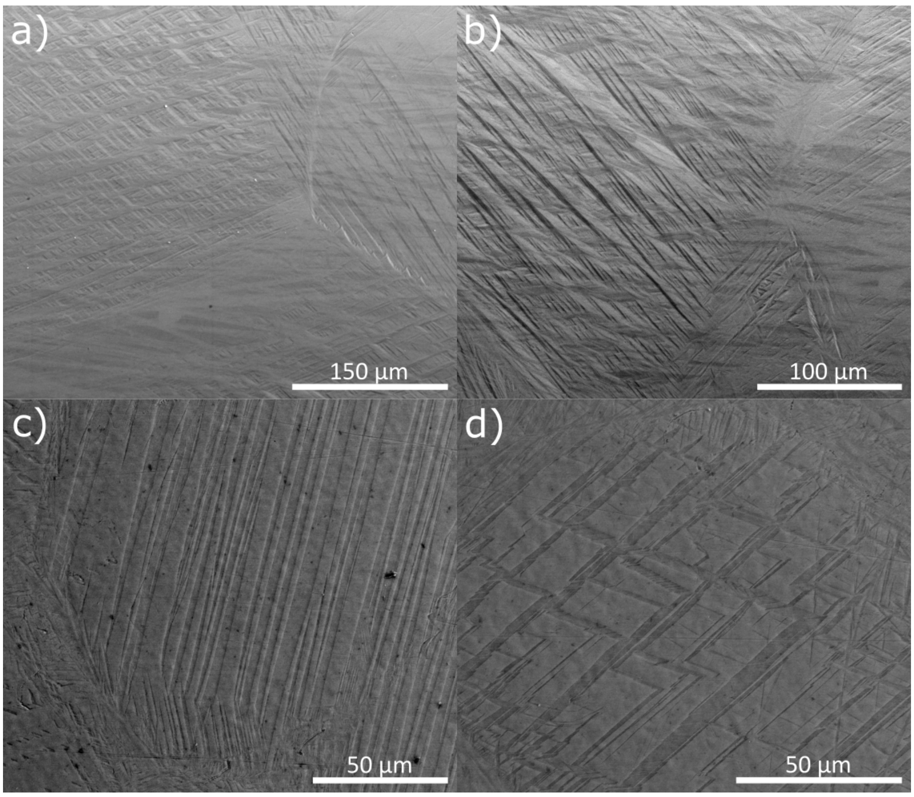

Figure 16: SEM micrograpghs of Ti-1023 specimens deformed in tension to 0.03 plastic strain at a strain rate of 10^{-1} s^{-1} in the a) and b) AQ and c) and d) MTS aged conditions